IJECBE (2026), 4, 1, 69–84
Received (29 April 2026) / Revised (13 June 2026)
Accepted (18 June 2026) / Published (30 March 2026)
https://doi.org/10.62146/ijecbe.v4i1.226
https://ijecbe.ui.ac.id
ISSN 3026-5258

International Journal of Electrical, Computer and Biomedical Engineering

RESEARCH ARTICLE

Experimental Characterization of a Tri-Axial FBG Accelerometer for Underwater Thruster-Induced Vibration Detection

Muhammad Alif Rahman Sukapraja[†], Retno Wigajatri Purnamaningsih[*†], Sasono Rahardjo[‡], Maristya Rahmadiansyah[‡], and Tinova Pramudya[‡]

†Department of Electrical Engineering, Faculty of Engineering, Universitas Indonesia, Depok, Indonesia
‡Research Center for Manufacturing Technology of Production Machinery, National Research and Innovation Agency (BRIN), Serpong, Indonesia
*Corresponding author. Email: retno.wigajatri@ui.ac.id

Abstract

Accurate underwater vibration measurement is essential for monitoring marine vehicles and submerged structures, yet conventional electrical accelerometers suffer from electromagnetic interference, waterproofing complexity, and signal degradation in harsh underwater environments. Although Fiber Bragg Grating (FBG) accelerometers excel in optical sensing, multi-axis FBG validations under realistic hydrodynamic excitation remain limited. This study addresses this problem by presenting a waterproof tri-axial Fiber Bragg Grating (FBG) accelerometer designed for underwater thruster-induced vibration detection. The sensor integrates three orthogonally arranged FBG elements within a compact, waterproof housing, enabling simultaneous measurement along the X, Y, and Z axes. Controlled experiments were conducted using a DC thruster under both free-air and submerged conditions. The results show that underwater operation significantly amplifies the Bragg wavelength shift ($\Delta\lambda_B$), with peak-to-peak variations increasing from 0.0044 nm in air up to 0.0267 nm on non-primary axes and 0.1005 nm on the excitation-aligned axis. The sensor also exhibits clear axis-dependent sensitivity, stable repeatability, and limited hysteresis, with a maximum hysteresis of 0.0053 nm ($\sim$ 5% of full-scale response). These findings demonstrate that the proposed tri-axial FBG platform provides sensitive, mechanically stable monitoring, offering critical experimental insights into fluid loading and multi-axis strain transfer.

Keywords: Fiber Bragg Grating, Tri-Axial Accelerometer, Underwater Vibration Sensing, Sensor Characterization, Thruster-Induced Vibration

1. Introduction

Reliable vibration sensing in underwater environments is an essential requirement for a wide range of engineering applications, including underwater vehicles, marine structures, and submerged mechanical systems. In practice, vibration information is often used to assess operational conditions, detect mechanical anomalies, and support monitoring tasks in harsh aquatic environments [1], [2], [3]. However, underwater sensing remains technically challenging due to high fluid density, complex hydrodynamic loading, and the susceptibility of conventional electrical sensors to electromagnetic interference and signal degradation [4], [5].

Conventional accelerometers based on micro-electromechanical systems (MEMS) [6], [7], [8], piezoelectric [9], [10], [11], piezoresistive [12], [13], [14], and capacitive [15], [16], [17] principles have been widely applied in vibration monitoring. While these sensors offer compact form factors and mature signal-conditioning techniques, their performance in underwater environments is often constrained by electromagnetic susceptibility, sealing requirements, and reduced signal fidelity under long cable transmission [18], [19]. These limitations motivate the exploration of alternative sensing technologies that are inherently robust to harsh environmental conditions.

FBG-based sensors have attracted increasing attention for underwater and subsea applications due to their intrinsic immunity to electromagnetic interference, high sensitivity, multiplexing capability, and compatibility with remote optical interrogation [20], [21], [22], [23]. FBG sensors have been successfully applied in air environment for strain [24], [25], [26], temperature in air environment [27], [28], [29], in water environment [30], [31], [32], pressure[33], [34], [35] , and acceleration measurements [36], [37], [38], and their lightweight structure makes them suitable for compact sensing systems [39]. In particular, FBG-based accelerometers have demonstrated promising performance for both static and dynamic measurements in laboratory [40] and field environments [41].

Despite these advantages, most existing studies on FBG accelerometers have focused primarily on single-axis sensing or on fundamental sensitivity enhancement through mechanical structure optimization [38], [42]. Theoretical investigations of FBG accelerometers using beam theory, modal analysis, and finite-element simulations have established a robust foundation for predicting cross-axis sensitivity and mechanical behaviors under idealized loading conditions [19], [36], [37], [38], [39], [40], [41]. However, these idealized models struggle to replicate the dynamic complexity of submerged operations. In underwater environments, sensor response is governed not only by internal structures but also by complex hydrodynamic effects, including added mass, fluid loading, and viscous damping [4], [5], [23]. Furthermore, the propagation of vibration is severely distorted by flow-induced noise, turbulence, and broadband acoustic interference generated by rotating propulsion systems, making precise signal isolation difficult. Consequently, while theoretical models are indispensable for guiding sensor design, systematic experimental validation remains essential to quantify these multi-axis coupling behaviors under realistic underwater excitations. Experimental investigations of multi-axis FBG accelerometers under realistic underwater excitation remain relatively limited. Moreover, the influence of fluid loading, vibration directionality, and source-sensor distance on the response of tri-axial FBG accelerometers has not been sufficiently explored through systematic experimental validation.

In underwater environments, vibration propagation is strongly affected by fluid density and mechanical coupling between the source and the surrounding medium. These factors introduce direction-dependent and distance-dependent variations in the mechanical strain transferred to the sensing element. Understanding these effects is critical for evaluating the practical applicability of multi-axis FBG accelerometers in underwater vibration monitoring systems, particularly when the vibration source is a rotating thruster or propeller commonly found in Autonomous Underwater Vehicles (AUVs) and marine platforms.

In our earlier work, a tri-axial FBG accelerometer was explored for the detection of vortex-induced vibrations generated by an underwater pump. The experimental results indicated that, under submerged conditions, increasing the distance between the vibration source and the sensor led to a systematic and approximately linear reduction in the measured Bragg wavelength shift ($\Delta\lambda_B$) [23]. Based on the preliminary observations, the present paper reports an engineering-oriented experimental characterization of a tri-axial FBG accelerometer subjected to thruster-induced vibrations under both free-air and underwater environments. The study emphasizes sensor configuration, experimental setup, and systematic validation rather than algorithmic localization or modelling accuracy. Comparative experiments are conducted to evaluate sensitivity differences between air and water, assess repeatability and hysteresis behavior, and examine the effects of source distance and orientation on sensor response. Physical interpretations are provided to explain observed trends in terms of fluid density, hydrodynamic loading, and mechanical coupling.

Through controlled laboratory experiments, the sensor demonstrates a pronounced increase in vibration sensitivity under submerged conditions, with measured $\Delta\lambda_B$ reaching approximately 0.0267 nm on the X-axis and up to 0.1005 nm on the axis directly aligned with the excitation, compared to only 0.0044 nm in free air. The sensor further exhibits stable repeatability and limited hysteresis, with a maximum hysteresis magnitude of 0.0053 nm (approximately 5% of full-scale wavelength shift) under cyclic loading.

By providing a comprehensive experimental assessment of tri-axial FBG accelerometer behavior under submerged excitation, this work aims to contribute practical insight into the deployment of optical fiber-based vibration sensors for underwater engineering applications.

2. Methodology

2.1 Fiber Bragg Grating

A Fiber Bragg Grating (FBG) is created by inscribing a periodic modulation of the core's refractive index along an optical fiber, forming a narrow-band reflector whose center wavelength depends on both the effective refractive index and the grating period. The first-order Bragg condition is given by [43], [44], [45]:

$$\lambda_B = 2n_{eff}\wedge \tag{1}$$

where λ_B is the Bragg wavelength, n_{eff} is the effective core index, and $\wedge$ is the grating period. When the grating is subjected to axial strain or a temperature change both effective core index and grating period shift, yielding a fractional Bragg-wavelength shift of [23]:

$$\frac{\Delta\lambda_B}{\lambda_B} = (1 - P_e)\varepsilon + (\alpha + \xi)\Delta T \tag{2}$$

where P_e is the effective photo-elastic coefficient, α is the thermal expansion coefficient, and ξ is the thermo-optic coefficient of the fiber.

2.2 Fiber Bragg Grating Accelerometer

A Fiber Bragg Grating (FBG) accelerometer couples a mechanical sensing element (e.g., a cantilever beam with a proof mass) to an FBG so that applied acceleration induces axial strain in the grating, producing a measurable shift in the λ_B. Ignoring temperature effects, the relationship between axial strain and Bragg-wavelength shift is derived from (2) by omitting the thermal term [46], [47]:

$$\Delta\lambda_B = \lambda_B(1 - P_e)\varepsilon \tag{3}$$

where λ_B is the unstrained Bragg wavelength and P_e is the effective photo-elastic coefficient.

In a typical three-axis FBG accelerometer, each axis sensor comprises a small seismic mass mounted on a flexural element of length, width, and thickness. Under a force, the induced axial strain in the beam is:

$$\varepsilon = \frac{6FL}{EBt^2} \tag{4}$$

with E is the Young's modulus of the beam material, L is the length of the beam, B is the width of the beam, and t is the thickness of the beam. Substituting (4) into (3) yields the wavelength shift as a direct function of applied force:

$$\Delta\lambda_B = (1 - P_e)\frac{6FL}{EBt^2}\lambda_B \tag{5}$$

2.3 Sensor Configuration

The sensing element employed in this study is a tri-axial FBG accelerometer (shown in Fig. 1) to capture vibration responses along three orthogonal directions. The sensor consists of three individual FBGs inscribed on single-mode optical fibers, each mounted to respond predominantly to axial strain along one spatial axis (X, Y, and Z). The three sensing axes are arranged orthogonally and integrated within a rigid, waterproof aluminium housing to ensure mechanical stability and protection under submerged conditions.

Each FBG is characterized by a distinct nominal λ_B to enable independent interrogation and prevent spectral overlap. The compact sensor structure is intended to minimize mass-induced distortion while maintaining sufficient stiffness for repeatable vibration transmission. This configuration allows simultaneous multi-directional

Figure 1. Three-axis Fiber Bragg Grating (FBG) accelerometer

vibration sensing while preserving the intrinsic advantages of optical fiber-based measurement, including electromagnetic immunity and remote interrogation capability.

2.4 Experimental Setup

A controlled experimental setup was developed to evaluate the vibration response of the tri-axial FBG accelerometer in both free-air and underwater environments. A DC thruster shown in Fig. 2 was used as a repeatable and controllable vibration source, representing a typical rotating propulsion mechanism encountered in underwater engineering applications.

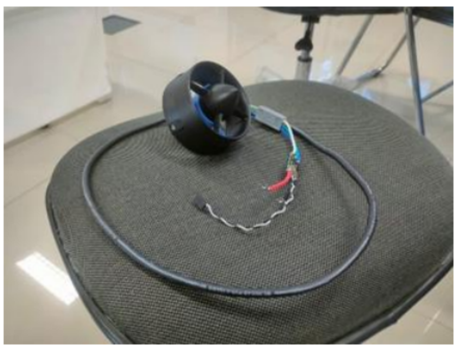

Figure 2. DC Thruster

The thruster was driven by pulse-width modulation (PWM) signals generated using a microcontroller-based control unit, enabling consistent adjustment of rotational speed and vibration intensity. Optical interrogation of the FBG sensors was performed using a broadband light source and an optical interrogator, which continuously monitored $\Delta\lambda_B$ induced by mechanical strain. All wavelength data were logged in real time using a computer-based acquisition system.

To ensure experimental consistency, the thruster was rigidly mounted on a fixed frame and mechanically isolated from the sensor support structure to minimize unintended structural coupling. The relative position between the thruster and the sensor was precisely controlled throughout all experiments. The flow diagram of the experimental setup is shown at Fig 3.

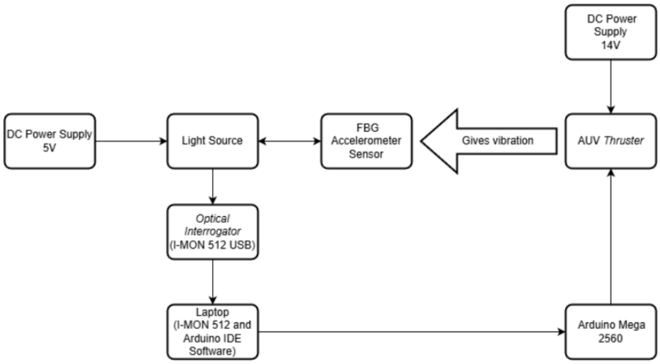

Figure 3. Experimental flow diagram

2.5 *Free-Air and Underwater Experiments*

Initial characterization was conducted in a free-air environment to establish baseline sensor behaviors and isolate vibration responses without fluid loading effects. During free-air testing, the thruster and sensor were placed on separate supports with sufficient spatial separation to prevent direct mechanical transmission. PWM excitation was applied incrementally and λ_B responses from all three sensing axes were recorded at a fixed sampling rate. The experimental setup schematic of the free-air experiment is shown at Fig. 4(a). Fig. 4(b) shows the photograph of the experimental setup.

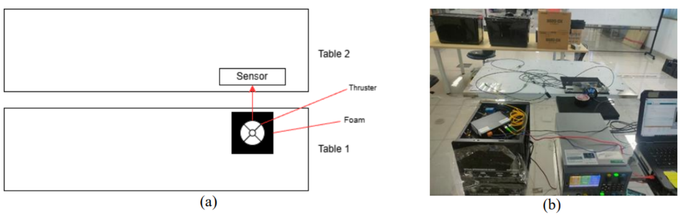

Figure 4. (a) Free-air experimental setup schematics (b) Photograph of experimental setup

Subsequently, identical experiments were repeated in an underwater environment using a freshwater test pool. Both the thruster and the sensor were fully submerged and secured at a fixed depth to maintain stable orientation and minimize buoyancy-induced motion. The same excitation sequence and data acquisition parameters used in free-air testing were applied underwater, allowing direct comparison between the two environments. Water temperature was maintained at a constant level to reduce thermal drift in the optical measurements. The schematic of the experimental setup is shown in Fig 5(a) and a photo of the experimental setup in the pond is shown in Fig 5(b).

2.6 *Sensitivity and Repeatability Evaluation*

Sensor sensitivity was evaluated by analyzing the magnitude of $\Delta\lambda_B$ induced by varying thruster excitation levels. For each PWM setting, multiple wavelength samples

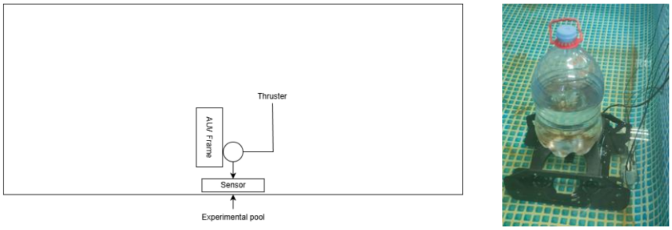

(a) (b)

Figure 5. (a) Underwater experimental setup schematics (b) Photograph of experimental setup

were collected to capture steady-state vibration behavior. Sensitivity was quantified as the range between maximum and minimum wavelength shifts observed across the excitation sequence.

Repeatability was assessed by examining the consistency of sensor responses under repeated excitation conditions. Multiple measurement cycles were conducted for each axis, and statistical dispersion of the wavelength data was analyzed to evaluate measurement stability.

2.7 Hysteresis Analysis

Hysteresis behavior was investigated through controlled loading-unloading experiments. In these tests, the thruster excitation level gradually increased in discrete steps and subsequently decreased following the same sequence. This procedure was repeated independently for each sensing axis by aligning the thruster with the corresponding sensor direction. The hysteresis test scheme, including three sensor positions, is shown in Fig. 6(a), and the photograph of position 1 is shown in Fig. 6(b).

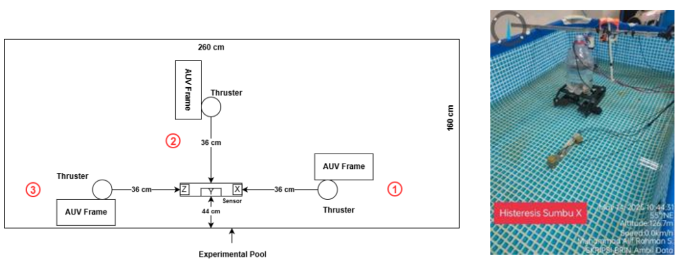

(a) (b)

Figure 6. (a) Thruster test scheme on tri-axial sensor (b) Experimental photo at X-axis sensor (position 1)

For each excitation level, wavelength data were recorded after allowing sufficient time for vibration stabilization. The median wavelength values were extracted and plotted against excitation level to visualize hysteresis loops. The maximum deviation between loading and unloading curves was used as an indicator of hysteresis magnitude.

2.8 Data Processing

All experimental data were processed offline using spreadsheet-based analysis tools. Transient data at the beginning of each measurement sequence were discarded to ensure that only stable vibration responses were evaluated. Median wavelength values were used to reduce the influence of short-term fluctuations. The processed data were subsequently used for comparative analysis between air and underwater conditions, as well as for evaluating sensitivity, hysteresis, and spatial response trends.

3. Results

3.1 Free-Air and Underwater Vibration Response

The vibration response of the tri-axial FBG accelerometer was first evaluated under free-air and underwater conditions to establish baseline behavior and assess the influence of the surrounding medium. Figure 7(a)–7(c) shows that λ_B fluctuations recorded in underwater experiments are consistently larger and more irregular compared to those observed in free-air tests. This behavior reflects the increased mechanical loading imposed by the surrounding fluid, which enhances the transmission of vibration-induced strain to the FBG sensing elements.

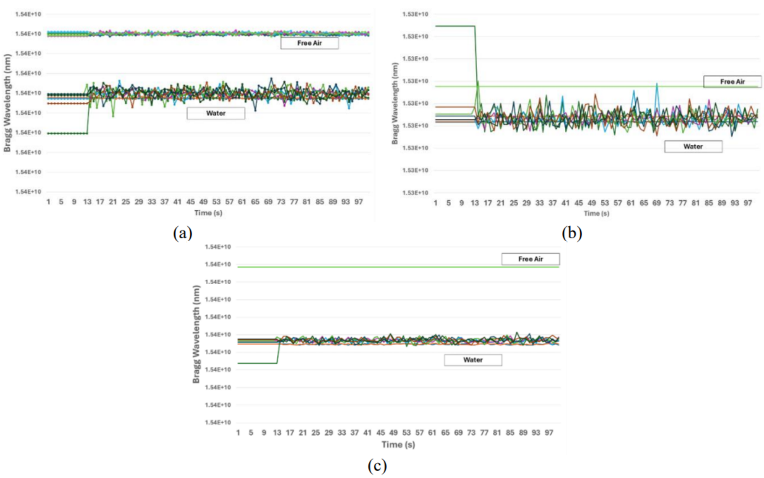

Figure 7. Graph of experimental data results in (a) X-Axis sensor (b) Y-Axis sensor (c) Z-Axis sensor

Quantitative comparison at Fig. 8(a) – Fig. 8(c) shows that the dynamic range of $\Delta\lambda_B$ in water is significantly greater than that measured in air across all sensing axes. In free-air conditions, wavelength variations remain relatively small and stable, whereas submerged operation produces larger peak-to-peak shifts.

3.2 Axis-Specific Sensitivity Characteristics

Distinct sensitivity characteristics were observed among the three sensing axes. The sensing axis directly aligned with the thruster exhibited the largest $\Delta\lambda_B$, indicating stronger mechanical coupling along the excitation direction, as shown in the axial-alignment response curves in Fig. 7. Conversely, sensing axes oriented obliquely or

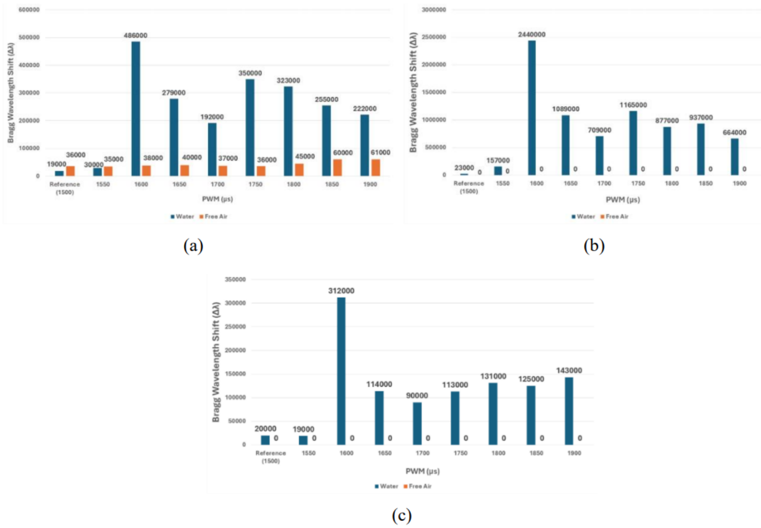

Figure 8. Wavelength shift range graphs for (a) X-axis, (b) Y-axis, and (c) Z-axis sensors

positioned farther from the vibration source exhibited reduced response magnitudes, consistent with the comparative trends observed across the multi-axis responses in Fig. 8(a) – Fig. 8(c).

In underwater tests, the Y-axis sensor consistently recorded the highest λ_B variation when the thruster was aligned along the same axis, as evidenced by the peak response amplitude shown in Fig 8(b). This behavior is attributed to direct exposure to vibration-induced fluid motion and reduced attenuation along the principal excitation direction. The X-axis and Z-axis sensors exhibited lower but still measurable wavelength responses under the same excitation conditions, reflecting anisotropic vibration propagation and axis-dependent strain transfer, as illustrated by the relative response levels in Fig. 8(a) and Fig. 8(c), respectively.

3.3 Sensitivity Enhancement in Submerged Conditions

Sensitivity analysis, defined by the difference between the maximum and minimum λ_B values, confirms a pronounced enhancement in sensor response under submerged conditions. As shown in Fig. 8(a) – Fig. 8(c), the peak-to-peak λ_B variation measured underwater is substantially larger than that observed in free-air operation for all sensing axes. This increase in sensitivity is attributed to the combined effects of increased fluid inertia, added mass loading on the sensor housing, and stronger mechanical coupling between the thruster-induced vibration field and the sensing structure, as evidenced by the comparative response amplitudes presented in Fig. 8(a) – Fig. 8(c).

These results indicate that the sensor exhibits greater responsiveness to vibration excitation in water than in air, underscoring the suitability of FBG-based accelerometers for underwater vibration monitoring applications where fluid–structure interaction plays a dominant role.

3.4 Repeatability and Hysteresis Behavior

Repeatability tests indicate that the tri-axial FBG accelerometer produces consistent wavelength responses under repeated excitation cycles. For identical thruster operating conditions, the recorded λ_B exhibit minimal variation, suggesting stable mechanical behavior and reliable strain transfer to the FBG elements.

Hysteresis analysis further reveals limited hysteresis effects across all sensing axes. When excitation levels were gradually increased and subsequently decreased, the resulting loading–unloading curves formed narrow hysteresis loops. The maximum hysteresis magnitude remained small relative to the overall wavelength shift range, indicating that the sensor maintains good reversibility and mechanical stability under cyclic vibration loading. Slightly larger hysteresis values were observed for the axis directly facing the thruster, which can be attributed to stronger hydrodynamic forces and localized fluid flow effects.

From the three graphs shown at Fig. 9(a) – Fig. 9(c), the maximum hysteresis values of the three X-Axis, Y-Axis, and Z-Axis sensors respectively when the thruster position is on the same axis as the X-Axis sensor are 0.00015 nm, 0.00055 nm, and 0.0002 nm. The average of the three maximum hysteresis values is 0.0003 nm so that when the thruster is placed on the same axis as the X-Axis sensor, the hysteresis of the three sensors is very small.

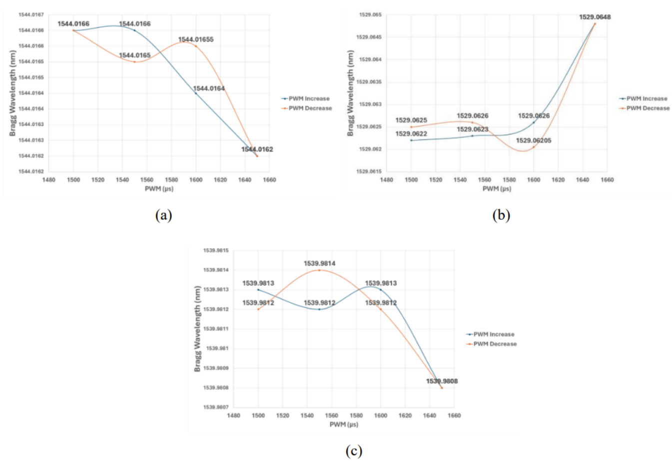

Figure 9. Hysteresis graph of (a) X-Axis sensor (b) Y-Axis sensor (c) Z-Axis sensor when the thruster position is on the same axis as the X-Axis sensor

At Fig. 10(a) – Fig. 10(c), the maximum hysteresis values of the three X-Axis, Y-Axis, and Z-Axis sensors respectively when the thruster position is on the same axis as the Y-Axis sensor are 0.0034 nm, 0.0045 nm, and 0.0053 nm. The average of the three maximum hysteresis values is 0.0044 nm. The average maximum hysteresis results of these three sensors are much greater than when the thruster position is on the same axis as the X-Axis sensor.

Fig. 11(a) – Fig. 11(c) shows the maximum hysteresis values of the three X-Axis, Y-Axis, and Z-Axis sensors respectively when the thruster position is on the same

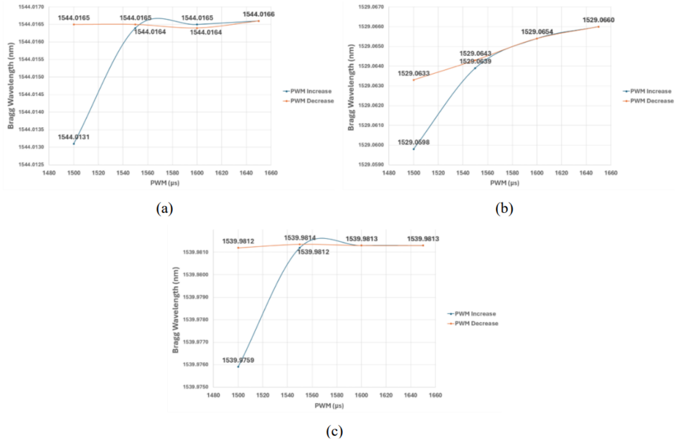

Figure 10. Hysteresis graph of (a) X-Axis sensor (b) Y-Axis sensor (c) Z-Axis sensor when the thruster position is on the same axis as the Y-Axis sensor

axis as the Z-Axis sensor are 0.0003 nm, 0.0004 nm, and 0.0002 nm. The average of the three maximum hysteresis values is 0.0003 nm. The average maximum hysteresis results are the same as when the thruster is placed on the same axis as the X-Axis sensor, which can be caused by the similarity of structure between the X-Axis and Z-Axis sensors.

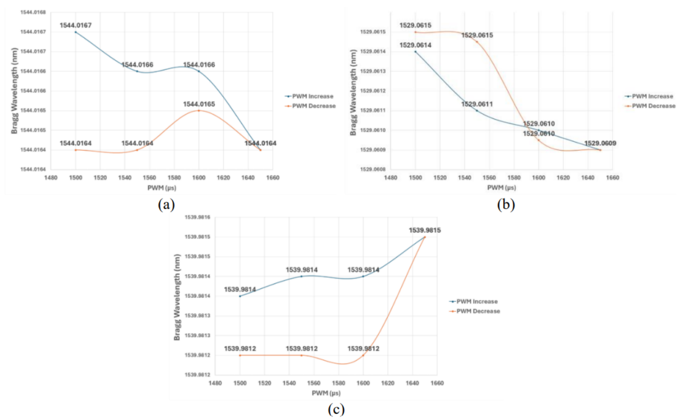

Figure 11. Hysteresis graph of (a) X-Axis sensor (b) Y-Axis sensor (c) Z-Axis sensor when the thruster position is on the same axis as the Z-Axis sensor

4. Discussion

The experimental results are consistent with the theoretical operating principle of an FBG accelerometer, in which mechanical vibration is converted into axial strain on the grating and subsequently appears as a shift in the Bragg wavelength. According to the

Bragg condition expressed in Eq. (1), the reflected wavelength depends on the effective refractive index and the grating period. When temperature effects are minimized, the dominant contribution to the wavelength shift arises from mechanically induced strain. Therefore, a larger measured $\Delta\lambda_B$ indicates that a larger strain has been transferred from the vibrating structure to the FBG element.

In the present experiment, the free-air test produced only a small peak-to-peak wavelength shift of approximately 0.0044 nm across all axes. This low response is theoretically reasonable because air has a low density and weak mechanical coupling with the thruster-induced vibration field. Under this condition, only limited vibration energy is transferred from the rotating thruster to the sensor housing, resulting in relatively small axial strain in the FBG elements. The free-air result can therefore be regarded as the baseline response of the sensor under weak fluid loading.

By contrast, the underwater experiment produced a substantially larger wavelength response, with $\Delta\lambda_B$ reaching approximately 0.0267 nm on non-primary axes and up to 0.1005 nm on the axis directly aligned with the thruster excitation. This result closely agrees with fluid–structure interaction theory. Water has a much higher density than air, so the rotation of the thruster generates stronger hydrodynamic forces, pressure fluctuations, and flow-induced vibration around the sensor. These effects increase the effective inertial loading (added mass) acting on the sensor housing and significantly improve the mechanical coupling between the excitation source and the FBG sensing structure, thereby amplifying the vibration-induced strain.

However, the larger and more irregular underwater response should be interpreted as the combined effect of enhanced fluid-structure coupling and superimposed measurement disturbances. In underwater environments, the propagation of vibration is inherently accompanied by hydrodynamic noise. Specifically, noise from turbulent flow, thruster rotation, local cavitation, mounting vibration, and optical interrogation may influence the measured wavelength response by reducing signal stability and obscuring weak vibration components. This explains the presence of fluctuations and minor irregularities in the underwater spectra compared to the stable free-air baseline.

The larger underwater response should not be interpreted only as higher sensor sensitivity in a simple static sense, but rather as the combined outcome of sensor sensitivity and stronger excitation transfer through the water medium. The FBG itself follows the same strain-wavelength relationship in both air and water. However, the underwater environment provides a more effective pathway for transferring thruster-induced forces to the sensor structure. This distinction is important because it shows that the measured enhancement arises from the interaction between the sensor, the excitation source, and the surrounding fluid, rather than from a change in the optical principle of the FBG.

The axis-dependent response observed in the experiment also follows the theoretical expectation of a tri-axial accelerometer. Each FBG element is arranged to respond predominantly to strain along one principal direction. When the thruster is aligned with a particular sensing axis, the vibration force component along that axis becomes dominant. As a result, the corresponding FBG experiences greater axial strain and produces a larger wavelength shift. Conversely, sensors positioned away from the principal excitation direction receive only secondary or oblique vibration components, leading to smaller $\Delta\lambda_B$ values. This explains why the axis directly facing the thruster exhibited the highest response, while the other axes still recorded measurable but lower wavelength variations. The response is therefore not random but reflects the directional nature of vibration transmission in a tri-axial sensing configuration.

The hysteresis results further support the mechanical reliability of the sensor. The maximum hysteresis value observed in the experiment was approximately 0.0053 nm, corresponding to about 5% of the maximum full-scale underwater wavelength shift of 0.1005 nm. From a theoretical perspective, low hysteresis indicates that the sensor structure behaves predominantly within the elastic region during cyclic excitation. In other words, when the excitation is increased and then decreased, the strain transferred to the FBG follows a largely reversible path. The absence of large hysteresis suggests that permanent deformation, bonding slippage, or mechanical instability inside the sensor housing is limited. This is an important result for underwater vibration monitoring because it indicates that the sensor can provide repeatable measurements under repeated loading conditions.

The slightly higher hysteresis observed when the thruster was aligned with the most responsive axis can be attributed to stronger localized hydrodynamic loading. In this configuration, the sensor is exposed to the highest vibration intensity and more direct flow disturbance. Such loading may generate minor asymmetry between the loading and unloading paths, especially due to transient flow effects, local turbulence, and small variations in vibration coupling. However, because the hysteresis remains small relative to the full-scale response, the overall sensor behaviors can still be considered stable and suitable for practical monitoring applications.

Overall, the experimental findings agree well with the theoretical model of an FBG accelerometer. The measured wavelength shifts follow the expected relationship between mechanical excitation, induced strain, and Bragg wavelength modulation. The stronger underwater response is consistent with the higher density and stronger hydrodynamic coupling of water compared with air. The axis-dependent response confirms that the tri-axial configuration can distinguish the dominant direction of vibration excitation. Finally, the low hysteresis demonstrates that the sensor maintains reversible and repeatable behaviors under cyclic underwater vibration. These results collectively validate the tri-axial FBG accelerometer as a feasible sensing platform for underwater thruster-induced vibration detection.

5. Conclusion

This study has presented an experimental engineering validation of a tri-axial FBG accelerometer for underwater vibration sensing using a thruster-induced excitation source. Comparative testing in free-air and underwater environments demonstrates that the sensor exhibits a substantially stronger response when submerged, confirming its suitability for vibration measurements in fluid-loaded conditions.

The tri-axial configuration enables simultaneous multi-directional vibration sensing and reveals clear differences in response magnitude associated with excitation alignment and source-sensor separation. The sensor shows stable and repeatable behavior under cyclic excitation, with limited hysteresis relative to its full-scale response, indicating reliable mechanical performance for practical monitoring applications.

Overall, the results demonstrate that tri-axial FBG accelerometers provide a robust and sensitive platform for underwater vibration monitoring, particularly in scenarios involving rotating propulsion sources such as thrusters. The experimental characterization presented in this work offers a practical basis for future studies, including extended field deployment, integration with multi-sensor arrays, or the development of advanced signal interpretation methods for more complex underwater monitoring systems.

Acknowledgement

This research was supported by Program Riset dan Inovasi untuk Indonesia Maju (RIIM) LPDP Grant and BRIN, grant number (G3) No: RIIM-30141557602.

References

[1] I. U. Hassan, K. Panduru, and J. Walsh. "An In-Depth Study of Vibration Sensors for Condition Monitoring". In: *Sensors* 24.3 (Jan. 2024), p. 740. DOI: 10.3390/s24030740.

[2] X. Huang et al. "A Low-Frequency Vibration Sensor Based on Ball Triboelectric Nanogenerator for Marine Pipeline Condition Monitoring". In: *Sensors* 24.12 (June 2024), p. 3817. DOI: 10.3390/s24123817.

[3] D. Xiao et al. "The Design and Data Analysis of an Underwater Seismic Wave System". In: *Sensors* 25.13 (July 2025), p. 4155. DOI: 10.3390/s25134155.

[4] A. M. Skålvik et al. "Challenges, Limitations, and Measurement Strategies to Ensure Data Quality in Deep-Sea Sensors". In: *Frontiers in Marine Science* 10 (2023), p. 1152236. DOI: 10.3389/fmars.2023.1152236.

[5] R. J. Taher and K. K. Mohsen. "Underwater Wireless Sensor Networks (Review)". In: *BIO Web of Conferences* 97 (2024), p. 00023. DOI: 10.1051/bioconf/20249700023.

[6] M. B. Tayl et al. "Innovative Hybrid Analysis for Underwater MEMS Sensor Imitating Veterinary Cilia Optimum Structure". In: *Ain Shams Engineering Journal* 15.1 (2024), p. 102283. DOI: 10.1016/j.asej.2023.102283.

[7] C. Tu et al. "A Bent-TBTF Resonant MEMS Accelerometer Using Auxiliary Supporting Beams". In: *IEEE Electron Device Letters* 45.11 (2024), pp. 2177–2180. DOI: 10.1109/LED.2024.3453324.

[8] S. Tez et al. "A Bulk-Micromachined Three-Axis Capacitive MEMS Accelerometer on a Single Die". In: *Journal of Microelectromechanical Systems* 24.5 (2015), pp. 1264–1274. DOI: 10.1109/JMEMS.2015.2451079.

[9] L. Guo et al. "Piezoelectric Wavy Whisker Sensor for Perceiving Underwater Vortex from a Bluff Body". In: *Sensors and Actuators A: Physical* 365 (2024), p. 114875. DOI: 10.1016/j.sna.2023.114875.

[10] B. Hu et al. "A Novel Trapezoidal ScAlN/AlN-Based MEMS Piezoelectric Accelerometer". In: *IEEE Sensors Journal* 21.19 (2021), pp. 21277–21284. DOI: 10.1109/JSEN.2021.3101219.

[11] A. Unnikrishnan et al. "Design of 3-Axis Piezoelectric Accelerometer for Body Activity Measurements". In: *International Conference on Advances in Computing, Communication and Systems*. Coimbatore, India, 2022, pp. 1726–1730. DOI: 10.1109/ICACCS54159.2022.9785278.

[12] E. Cabruja et al. "Piezoresistive Accelerometers for MCM-Package – Part II: The Packaging". In: *Journal of Microelectromechanical Systems* 14.4 (Aug. 2005), pp. 806–811. DOI: 10.1109/JMEMS.2005.845456.

[13] H.-S. Hsieh et al. "A Novel Stress Isolation Guard Ring Design for the Improvement of Three-Axis Piezoresistive Accelerometer". In: *Transducers 2011*. Beijing, China, 2011, pp. 1412–1415. DOI: 10.1109/TRANSDUCERS.2011.5969582.

[14] C.-H. Peng and M. S.-C. Lu. "Design and Characterization of CMOS Micromachined Piezoresistive Accelerometers". In: *IEEE Sensors Journal* 24.3 (2024), pp. 2500–2506. DOI: 10.1109/JSEN.2023.3340864.

[15] J. Chae, H. Kulah, and K. Najafi. “A Monolithic Three-Axis Micro-g Micromachined Silicon Capacitive Accelerometer”. In: *Journal of Microelectromechanical Systems* 14.2 (2005), pp. 235–242. DOI: 10.1109/JMEMS.2004.839347.

[16] A. Utz et al. “A High-Precision and High-Bandwidth MEMS-Based Capacitive Accelerometer”. In: *IEEE Sensors Journal* 18.16 (2018), pp. 6533–6539. DOI: 10.1109/JSEN.2018.2849873.

[17] H.-Y. Chiu et al. “Single-Axis Capacitive Accelerometer Chip with AC Offset Suppression Loop”. In: *Proceedings of the IEEE International Symposium on Circuits and Systems (ISCAS)*. Austin, TX, USA, 2022, pp. 2397–2400. DOI: 10.1109/ISCAS48785.2022.9937688.

[18] L. C. Lavau, M. Suhrke, and P. Knott. “Susceptibility of Sensors to IEMI Attacks”. In: *IEEE International Symposium on Electromagnetic Compatibility, Signal and Power Integrity*. Raleigh, NC, USA, 2021, pp. 533–537. DOI: 10.1109/EMC/SI/PI/EMCEurope52599.2021.9559197.

[19] Y. Chen et al. “Design and Experimental Validation of an FBG Accelerometer Using Cantilever-Hinge Structures”. In: *Optical Fiber Technology* 91 (2025), p. 104156. DOI: 10.1016/j.yofte.2025.104156.

[20] A. Bialiayeu. *The Sensitivity Enhancement of Tilted Fibre Bragg Grating Sensors with Polarization Dependent Resonant Nano-Scale Coatings*. 2015. DOI: 10.48550/arXiv.1502.04961. arXiv: 1502.04961.

[21] C.-Y. Hong et al. “Application of FBG Sensors for Geotechnical Health Monitoring, a Review of Sensor Design, Implementation Methods and Packaging Techniques”. In: *Sensors and Actuators A: Physical* 244 (2016), pp. 184–197. DOI: 10.1016/j.sna.2016.04.033.

[22] X. Zhao et al. “Research Progress in Fiber Bragg Grating-Based Ocean Temperature and Depth Sensors”. In: *Sensors* 25.1 (2025), p. 183. DOI: 10.3390/s25010183.

[23] J. M. K. Gani, R. W. Purnamaningsih, and S. Rahardjo. “Characterization of Fiber Bragg Grating Accelerometer for Underwater Vibration Detection”. In: *Jurnal Penelitian Pendidikan IPA* 10.6 (2024), pp. 3221–3227. DOI: 10.29303/jppipa.v10i6.7760.

[24] R. C. Anwar et al. “Analysis of Bare Uniform Fiber Bragg Grating Sensor for Measuring Strain on the Landing Gear of the LSU-02 Unmanned Aircraft”. In: *International Journal of Electrical, Computer, and Biomedical Engineering* 2.3 (2024). DOI: 10.62146/ijecbe.v2i3.70.

[25] X. X. Tang et al. “Applications of Fiber Bragg Grating in Strain Measurement of Concrete Bridge”. In: *Advanced Materials Research* 368–373 (2011), pp. 2286–2290. DOI: 10.4028/www.scientific.net/AMR.368-373.2286.

[26] C. E. Campanella et al. “Fibre Bragg Grating Based Strain Sensors: Review of Technology and Applications”. In: *Sensors* 18.9 (2018), p. 3115. DOI: 10.3390/s18093115.

[27] C. G. Ferro et al. “Experimental Development and Evaluation of a Fiber Bragg Grating-Based Outside Air Temperature Sensor for Aircraft Applications”. In: *Transportation Engineering* 14 (2023), p. 100214. DOI: 10.1016/j.treng.2023.100214.

[28] S. Daud and A. F. Ahmad Noorden. “Fibre Bragg Grating Sensor System for Temperature Application”. In: *Jurnal Teknologi* 78.3 (2016). DOI: 10.11113/jt.v78.7462.

[29] Z. X. Wu et al. “Research of the Technology Based on Fiber Bragg Grating for Measurement of Temperature Rise of Electrical Appliances”. In: *Advanced Materials Research* 571 (2012), pp. 200–204. DOI: 10.4028/www.scientific.net/AMR.571.200.

[30] I. Kustianto et al. “Water Temperature Measurement Using Fiber Bragg Grating”. In: *Jurnal Penelitian Pendidikan IPA* 9.11 (2023), pp. 9341–9345. DOI: 10.29303/jppipa.v9i11.3972.

[31] X. Zhao et al. “Temperature and Depth Sensor Based on Fiber Bragg Gratings with Temperature-Compensated Structure in Marine Environment”. In: *Coatings* 15.7 (2025), p. 795. DOI: 10.3390/coatings15070795.

[32] L. Wang et al. “A High Spatial Resolution FBG Sensor Array for Measuring Ocean Temperature and Depth”. In: *Photonic Sensors* 10.1 (2020), pp. 57–66. DOI: 10.1007/s13320-019-0550-0.

[33] N. A. Madani et al. “Detection of Low Hydrostatic Pressure Using Fiber Bragg Grating Sensor”. In: *International Journal of Technology* 14.7 (Dec. 2023), p. 1527. DOI: 10.14716/ijtech.v14i7.6714.

[34] S.-C. Her and S.-Z. Weng. “Fiber Bragg Grating Pressure Sensor Integrated with Epoxy Diaphragm”. In: *Sensors* 21.9 (May 2021), p. 3199. doi: 10.3390/s21093199.

[35] J. Lao et al. “Liquid Pressure Sensor Based on Fiber Bragg Grating with an Adjustable Structure”. In: *Sensors* 22.23 (Nov. 2022), p. 9188. doi: 10.3390/s22239188.

[36] Z. Li et al. “A Medium-Frequency Fiber Bragg Grating Accelerometer Based on Flexible Hinges”. In: *Sensors* 21.21 (Oct. 2021), p. 6968. doi: 10.3390/s21216968.

[37] X. Luo et al. “Fiber Bragg Grating Accelerometer Based on Symmetrical Double Flexure Hinges”. In: *Optical Fiber Technology* 68 (Jan. 2022), p. 102795. doi: 10.1016/j.yofte.2021.102795.

[38] Y. Wang et al. “Design and Analysis of a High-Sensitivity FBG Accelerometer with a Flexural Bearing”. In: *Measurement* 242 (Jan. 2025), p. 116093. doi: 10.1016/j.measurement.2024.116093.

[39] Y. Gu et al. “A Flexible FBG Micro-Pressure Sensor Based on a Double-Opening Slatted Arch Structure”. In: *IEEE Sensors Journal* (2025), pp. 1–1. doi: 10.1109/JSEN.2025.3601715.

[40] W. Chang et al. “Fiber Bragg Grating Accelerometer Based on Asymmetric Shaped Flexible Hinge Structure”. In: *Optics Communications* 569 (Oct. 2024), p. 130855. doi: 10.1016/j.optcom.2024.130855.

[41] L. Hong et al. “Temperature-Insensitive FBG Acceleration Sensor Based on Strain Chirp Effect”. In: *Measurement and Control* 54.5–6 (May 2021), pp. 658–667. doi: 10.1177/00202940211001900.

[42] R. Diharja et al. “Enhanced Underwater Acoustic Sensing Using Bare-Type Fiber Bragg Grating and Circular Membrane Structures”. In: *2025 9th International Conference on Electrical, Electronics and Information Engineering (ICEEIE)*. IEEE, Sept. 2025, pp. 1–6. doi: 10.1109/ICEEIE66203.2025.11252302.

[43] I. B. Kwon et al. “Multiplexing of FBG Sensor by Light Source Intensity Modulation”. In: *Key Engineering Materials* 270–273 (Aug. 2004), pp. 2134–2139. doi: 10.4028/www.scientific.net/KEM.270-273.2134.

[44] A. Othonos et al. “Fibre Bragg Gratings”. In: *Wavelength Filters in Fibre Optics*. Springer Berlin Heidelberg, pp. 189–269. doi: 10.1007/3-540-31770-8_6.

[45] E. Al-Fakih, N. A. Abu Osman, and F. R. Mahamd Adikan. “The Use of Fiber Bragg Grating Sensors in Biomechanics and Rehabilitation Applications: The State-of-the-Art and Ongoing Research Topics”. In: *Sensors* 12.10 (Sept. 2012), pp. 12890–12926. doi: 10.3390/s121012890.

[46] V. N. B. Chaluvadi and P. K. Pattnaik. “Effect of Strain and Temperature on FBG”. In: *2020 IEEE International Conference on Electronics, Computing and Communication Technologies (CONECCT)*. IEEE, July 2020, pp. 1–4. doi: 10.1109/CONECCT50063.2020.9198339.

[47] H.-D. Le et al. “Design a Fiber Bragg Grating Accelerometer-Based Using a Cantilever Beam Structure”. In: *2022 International Conference on Control, Robotics and Informatics (ICCRI)*. IEEE, Apr. 2022, pp. 43–47. doi: 10.1109/ICCRI55461.2022.00014.